10-9-2018

# Multielectron Redox Chemistry of Transition Metal Complexes Supported by a Non-Innocent N3P2 Ligand: Synthesis, Characterization, and Catalytic Properties

Denan Wang
*Marquette University*

Danushka M. Ekanayake
*Wayne State University*

Sergey V. Lindeman
*Marquette University*, sergey.lindeman@marquette.edu

Cláudio N. Verani
*Wayne State University*

Adam T. Fiedler
*Marquette University*, adam.fiedler@marquette.edu

Accepted version. *European Journal of Inorganic Chemistry*, Vol. 2018, No. 37 (October 9, 2018): 4133-4141. DOI. 

*European Journal of Inorganic Chemistry*, Vol. 2018, No. 37 (October 2018): 4133-4141. DOI. 

# Multielectron Redox Chemistry of Transition Metal Complexes Supported by a Non-Innocent $N_3P_2$ Ligand: Synthesis, Characterization, and Catalytic Properties

Denan Wang
Department of Chemistry, Marquette University, 53201 Milwaukee, Wisconsin,
Danushka M. Ekanayake
Department of Chemistry, Wayne State University, 5101 Cass Ave, 48202 Detroit, MI, United States
Sergey V. Lindeman
Department of Chemistry, Marquette University, 53201 Milwaukee, Wisconsin, United States
Cláudio N. Verani
Department of Chemistry, Wayne State University, 5101 Cass Ave, 48202 Detroit, MI, United States
Adam T. Fiedler
Department of Chemistry, Marquette University, 53201 Milwaukee, Wisconsin, United States

## Abstract

A new redox-active, diarylamido-based ligand ($\mathbf{L^{N3P2}}$) capable of $\kappa^5$-*N,N,N,P,P* chelation has been used to prepare a series of complexes with the general formula $[M^{II}(\mathbf{L^{N3P2}})]X$, where M = Fe (**1**; X = OTf), Co (**2**; X = $ClO_4$), or Ni (**3**;

X = $ClO_4$). The diarylamido core of monoanionic $\mathbf{L^{N3P2}}$ is derived from bis(2-amino-4-methylphenyl)amine, which undergoes condensation with two equivalents of 2-(diphenylphosphanyl)benzaldehyde to provide chelating arms with both arylphosphine and imine donors. X-ray structural, magnetic, and spectroscopic studies indicate that the $N_3P_2$ coordination environment generally promotes low-spin configurations. Three quasi-reversible redox couples between +1.0 and –1.5 V (vs. $Fc^+/Fc$) were observed in voltammetric studies of each complex, corresponding to $M^{II}/M^{III}$oxidation, $\mathbf{L^{N3P2}}$-based oxidation, and $M^{II}/M^{I}$ reduction (in order of highest to lowest potential). Spectroscopic and computational analyses of $\mathbf{3^{ox}}$ – generated via chemical one-electron oxidation of **3** – revealed that a stable diarylaminyl radical ($\mathbf{L^{N3P2\cdot}}$) is formed upon oxidation. The ability of the $Co^{II}$ complex (**2**) to function as an electrocatalyst for $H_2$generation was evaluated in the presence of weak acids. Moderate activity was observed using 4-*tert*-butylphenol as the proton source at potentials below –2.0 V. The insights gained here will assist in the future design of pentadentate mixed N/P-based chelates for catalytic processes.

# 1. Introduction

Recent studies have highlighted the ability of cobalt and nickel complexes to function as efficient electrocatalysts for environmentally significant reactions, such as $CO_2$ reduction[1] and $H_2$ generation.[2] Continued advances in this field depend upon the rational design of new and sophisticated ligand frameworks to enhance catalytic performance. By adjusting the ligand coordination environment, it is possible to tune the redox properties of the transition metal center, control the binding of substrates, and improve the overall stability of the catalyst. Moreover, these multielectron reactions can be facilitated by redox-active (i.e., “noninnocent”) ligands that actively participate in the catalytic mechanism by donating or accepting one or more electrons.[3]

Starting with the well-studied cobaloxime-based systems,[4] the large majority of cobalt catalysts for the hydrogen evolution reaction (HER) have employed ligands with only *N*-donors.[5] Examples include catalysts with tetra- or pentadentate polypyridyl ligands[6] and those featuring tetradentate Schiff-base macrocycles.[7, 8] While the development of HER catalysts with $CoN_4$ and $CoN_5$ structures has proven fruitful, there are potential advantages in using ligand scaffolds that also incorporate non-nitrogenous donors. To this end, the Verani and Fiedler labs have generated mono- and dinuclear cobalt HER catalysts, respectively, that feature multiple phenolate donors.[9] Of greatest relevance to the current study is the synthesis and catalytic characterization of the dicobalt complex shown in Scheme **1**, which is supported by the pentadentate ligand $\mathbf{L^{N3O2}}$. The trianionic $\mathbf{L^{N3O2}}$ chelate consists of a central diarylamido unit with two salicyaldimine arms, and reaction with $M^{II}$ ions yields homobimetallic complexes in which the diarylamido donor adopts a bridging position (Scheme **1**).[10] In 2017, we demonstrated that $[Co^{2+}_2(\mathbf{L^{N3O2}})(bpy)_2]ClO_4$ (bpy = 2,2’-bipyridine) serves as an efficient HER electrocatalyst in the presence of weak acids, employing a novel catalytic mechanism that involves cooperativity between the two cobalt centers.[9] Significantly, the $\mathbf{L^{N3O2}}$ ligand is redox-active due to the presence of the diarylamido unit, which undergoes reversible oxidation near 100 mV (vs. $Fc^{+/0}$).

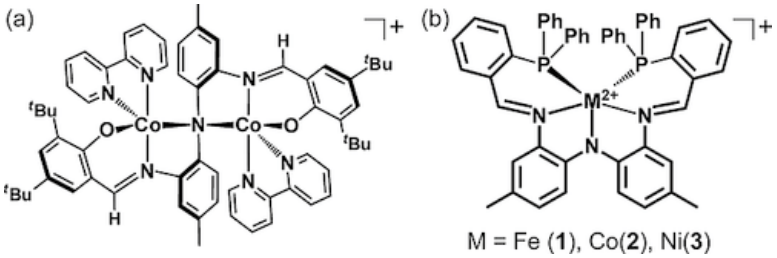


**Scheme 1**. (a) Dicobalt(II) complex with $\mathbf{L^{N3O2}}$ ligand. (b) $\mathbf{L^{N3P2}}$-based complexes **1**–**3**.

Building upon these efforts, we reckoned that replacement of the “hard” anionic phenolates of $\mathbf{L^{N3O2}}$ with “soft” neutral of phosphines would lower the redox potentials of the metal ion(s), making it possible to access the low oxidation and spin states required for the activation of electrophilic substrates (e.g., $CO_2$, $H^+$). We therefore prepared the monoanionic ligand $\mathbf{L^{N3P2}}$shown in Scheme **2**. $\mathbf{L^{N3P2}}$ can be considered the pentadentate analog of

the well-known PNP pincer ligands, which have been widely employed in both organometallic and inorganic chemistry.[11] Examples of pentadentate N3P2-ligands in the literature are relatively rare, but those reported by the Trovitch group exhibit interesting catalytic properties.[12] Moreover, a handful of complexes with mixed N/P ligation have proven to be effective catalysts for $H_2$production.[13]

This manuscript describes an initial survey of the coordination chemistry, electrochemical properties, and catalytic utility of the $\mathbf{L}^{N3P2}$ framework. Interestingly, reaction of $\mathbf{L}^{N3P2}$ with divalent transition-metal ions (M = Fe, Co, Ni) yields mononuclear complexes with the general formula $[M^{2+}(\mathbf{L}^{N3P2})]^{+}$, in contrast to the dinuclear complexes obtained with $\mathbf{L}^{N3O2}$. Despite this difference, the $\mathbf{L}^{N3P2}$-based complexes are promising candidates for HER catalysts for several reasons. Firstly, the coordination environment provided by $\mathbf{L}^{N3P2}$ is consistent with the design principles recently formulated by Brooker and co-workers for cobalt HER catalysts with Schiff-based ligands.[8] This study noted the improved performance of five-coordinate complexes (relative to 4C analogs) and the advantage of five-membered chelate rings, which is fully consistent with our previous findings.[9] We also hypothesized that the noninnocent nature of the diarylamido unit could reveal a mechanistic alternative to the $Co^{I}/Co^{III}$ cycle employed by most HER catalysts. Therefore, we have explored the electrocatalytic activity of the $\mathbf{L}^{N3P2}$-based cobalt complex (**2**) in the presence of weak acids. The results of these investigations are presented below.

# 2. Results and Discussion

## Synthesis and Molecular Structures

The red pro-ligand H$\mathbf{L}^{N3P2}$ was prepared by the condensation of bis(2-amino-4-methylphenyl)amine[10] with two equivalents of 2-(diphenylphosphanyl)benzaldehyde in toluene.[14] Treatment of H$\mathbf{L}^{N3P2}$ with the appropriate $M^{II}X_2$ salt (X = $ClO_4^-$ or $TfO^-$) in a 1:1 mixture of $CH_2Cl_2$ and MeCN, followed by addition of base, generated the dark brown complexes **1**–**3**. Crystals suitable for crystallographic studies were obtained by slow evaporation of 1:1 $CH_2Cl_2$/MeCN solutions. The solid-state structures of **1**–**3** were determined using X-ray crystallography, and details regarding the diffraction experiments and structure refinements are provided in Table S1. The unit cell of **1** contains two symmetry-independent complexes, in addition to unresolved solvent molecules (likely $CH_2Cl_2$). One of the two complexes is totally disordered due to superposition of enantiomers along a common (non-crystallographic) twofold axis. In addition, the presence of 2.6 triflate counteranions in the unit cell (1.3 per Fe) suggests that the Fe complex has been partially oxidized to the corresponding dication. While these factors limited the resolution of the structure of **1**, the Fe–N/P bond lengths are accurate to within 0.01 Å for the non-disordered complex.

Figure 1 (a) displays the $[Co(\mathbf{L}^{N3P2})]^{+}$ unit found within the structure of **2**, which is representative of the **1**–**3** series. In all three structures, the five-coordinate $M^{II}$ center exists in a distorted trigonal-bipyramidal (TBP) coordination environment with the imine *N*-donors (N2 and N3) occupying the axial positions. The equatorial plane is constituted by the diarylamido (N1) and phosphine (P1/P2) donors, and the sum of the resulting angles around the $M^{II}$ centers is almost exactly 360°. The overlay of solid-state geometries shown in Figure 1(b) highlights the large degree of structural similarity between the three complexes. The axial M1–N2/N3 distances vary only slightly across the series (average value of 1.92 ± 0.03 Å), while the M1–N1 bond lengths are confined between 1.83 and 1.91 Å (Table 1). Larger deviations are observed with respect to the positions of the phosphine donors: the M1–P1/P2 bond lengths range between 2.155 and 2.252 Å, following the order Fe(**1**) < Co(**2**) < Ni(**3**). The corresponding P1–M1–P2 angles vary from 97 to 110° in the same order.

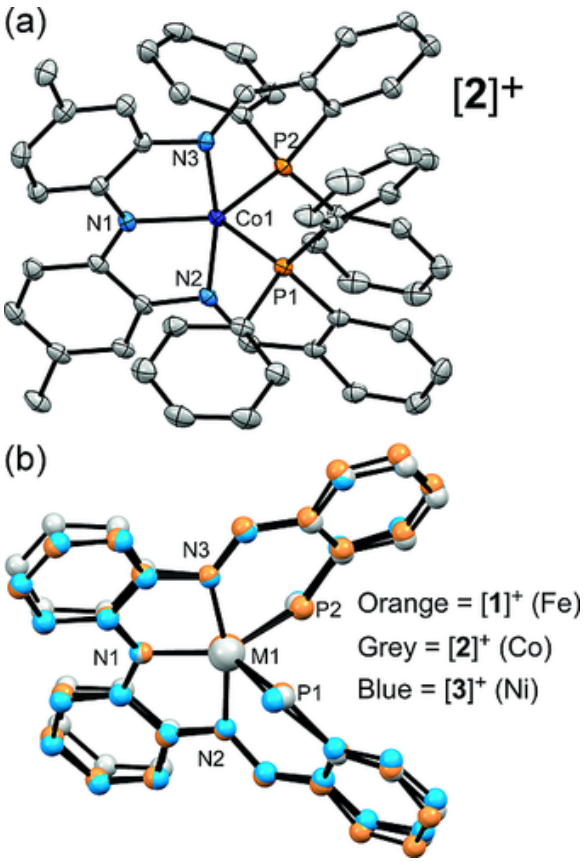


**Figure 1**. (a) Thermal ellipsoid plot (50 % probability) obtained from the X-ray crystal structure of complex **2**. The $ClO_4^-$ counteranion is not shown. (b) Overlays of the crystallographic structures of complexes **1** (orange), **2** (grey), and **3**(blue). The phenyl and methyl substituents of the $\mathbf{L^{N3P2}}$ ligand have been omitted for clarity.

**Table 1.** Selected bond lengths [Å] and bond angles [°] for complexes **1**–**3** as determined by X-ray crystallography

| | **1**[a] | **2** | **3** |
|---|---|---|---|
| | **[M = Fe]** | **[M = Co]** | **[M = Ni]** |
| M1–N1 | 1.834(3) | 1.8652(15) | 1.9086(16) |
| M1–N2 | 1.945(3) | 1.9258(15) | 1.8961(16) |
| M1–N3 | 1.949(3) | 1.9169(15) | 1.9074(16) |
| M1–P1 | 2.1546(13) | 2.2121(5) | 2.2522(5) |
| M1–P2 | 2.1578(11) | 2.2169(5) | 2.2471(5) |
| M1–L (ave) | 2.008 | 2.027 | 2.042 |
| N1–M1–N2 | 83.71(15) | 83.72(6) | 83.50(7) |
| N1–M1–N3 | 83.71(15) | 83.75(6) | 83.81(7) |
| N1–M1–P1 | 131.60(11) | 125.24(5) | 126.13(5) |
| N1–M1–P2 | 130.97(11) | 131.54(5) | 123.37(5) |
| N2–M1–N3 | 167.36(14) | 167.24(6) | 167.07(7) |
| N2–M1–P1 | 91.12(10) | 89.42(5) | 92.43(5) |
| N2–M1–P2 | 96.64(11) | 98.00(5) | 95.26(5) |
| N3–M1–P1 | 98.11(9) | 95.85(5) | 97.06(5) |
| N3–M1–P2 | 90.73(11) | 92.12(5) | 89.64(5) |
| P1–M1–P2 | 97.43(5) | 103.22(2) | 110.49(2) |
| tau-value | 0.60 | 0.60 | 0.68 |

[a] The unit cell of complex **1** contains two symmetry-independent iron complexes, one of which is highly disordered. The metric parameters shown here correspond to the non-disordered complex.

A survey of related TBP complexes with mixed N/P ligation[13],[15] reveals that the short axial M1–N2/N3 bond lengths (1.92 ± 0.03 Å) of **1**–**3** are characteristic of low-spin ground states. This conclusion is supported by solid-

state magnetic susceptibility measurements. Complex **2** was found to possess a magnetic moment of 1.7 $\mu_B$ – typical of a $S$ = 1/2 paramagnet – while complexes **1** and **3** yielded effective magnetic moments near zero. The slight paramagnetism observed for **1** (0.30 $\mu_B$) is likely due to small amounts of the one-electron oxidized complex (**1**$^{ox}$), as apparent in the crystal structure.

## Spectroscopic Features

Complexes **1**–**3** are a dark brown color due to a series intense ($\varepsilon$ > 5000 $M^{-1}cm^{-1}$) bands across the visible region arising from $\mathbf{L}^{N3P2}$-based and charge transfer transitions (Figure S1). The $^1$H NMR spectrum of **1** in $CD_2Cl_2$ consists of a series of sharp peaks in the region between 0 and 10 ppm (Figure S2), indicative of a diamagnetic electronic structure. Similarly, the Co$^{II}$ center of **2** remains low-spin in solution, as evident by the magnetic moment of 1.7 $\mu_B$ measured using the Evans method[16] in $CH_2Cl_2$ at room temperature. The X-band EPR spectrum of **2** in frozen $CH_2Cl_2$ at 10 K (Figure **2**) revealed a nearly axial $S$ = 1/2 signal ($g_x$ = 2.054, $g_y$ = 2.063, $g_z$ = 2.131), featuring hyperfine splitting from multiple nuclei. A satisfactory simulation of this complex spectrum was obtained with the aid DFT calculations, which provided initial sets of $A$-values and Euler angles for the hyperfine tensors of the Co and P nuclei. The spin-Hamiltonian parameters used in the final simulation are given in the caption of Figure **2**. Contributions from both $^{59}$Co and $^{31}$P nuclei are necessary to account for the abundance of observed hyperfine features. Consistent with DFT calculations of **2**, the **A**-tensor of the $^{59}$Co nucleus ($I$ = 7/2) is highly anisotropic with the largest component ($A_{zz}^{Co}$ = 85 G) aligned in the $g_z$-direction. The $A$-tensors of the two quasi-equivalent $^{31}$P nuclei ($I$ = 1/2) are more isotropic ($A^P$ ≈ 60 G). The EPR spectrum of **2** follows the pattern of $g_{\|} > g_{\perp} > 2.00$ and $A_{\|}^{Co} >> A_{\perp}^{Co}$ observed for other Co$^{II}$complexes with trigonal-bipyramidal geometry.[17] This pattern indicates that the unpaired electron of **2** resides in a Co($d_{x^2-y^2}$)-based orbital lying in the equatorial plane, as supported by DFT calculations (Figure **2**, inset).

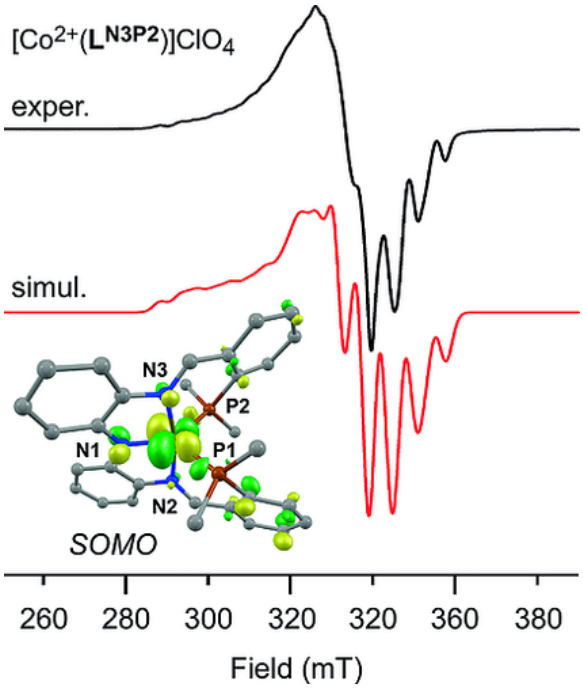


**Figure 2**. X-band EPR spectrum (black line) of complex **2** in frozen $CH_2Cl_2$. Parameters: frequency = 9.631 GHz; power = 2.0 mW; modulation amplitude = 1.0 G; $T$ = 10 K. The simulated spectrum (red line) was obtained with the following spin-Hamiltonian parameters: $g_{x,y,z}$ = 2.054, 2.063, 2.131; ($^{59}$**Co**): $A$ = [3.6, 18, 89] G; Euler angles = [0°, 0°, 60°]. ($^{31}$**P1**): $A$ = [71, 64, 64] G; Euler angles = [0°, 0°, 20°]. ($^{31}$**P2**): $A$ = [43, 43, 64] G; Euler angles = [0°, 80°, –50°]. *Inset*: Isosurface plots of the Co($d_{x^2-y^2}$)-based MOs of complex **2** ($S$ = 1/2) generated from DFT calculations. The phenyl substituents of the phosphine donors were replaced by methyl groups.

Interestingly, the $^{1}$H NMR spectrum of **3** measured at room temp. in $CD_2Cl_2$ exhibits broad, paramagnetically-shifted peaks at 91, 57, 33 and –77 ppm (Figure S3). Using the Evans method, the magnetic moment was found to be 2.80 $\mu_B$ in solution, near the theoretical spin-only value of 2.83 $\mu_B$ for a $S$ = 1 paramagnet. Thus, the spin-state of $Ni^{II}$-containing **3** changes from low-spin to high-spin upon dissolving in $CH_2Cl_2$. To determine whether the solvated complex exhibits spin-crossover behavior, $^{1}$H NMR spectra were measured at multiple temperatures (25, –40, and –90 °C). As the temperature decreases, the peaks shift linearly away from the diamagnetic region (Figure S3), exhibiting the Curie behavior ($\delta \propto T^{-1}$) characteristic of paramagnetic complexes. Thus, complex **3** remains in the high-spin state across the temperature range studied here. Crystal packing effects likely account for the prevalence of more compact low-spin structure in the crystalline phase.

## Electrochemical Properties

Voltammetric methods were used to probe the electron-transfer abilities of complexes **1**–**3** in $CH_2Cl_2$ solutions with 100 mM $(NBu_4)PF_6$ as the supporting electrolyte. Multiple redox events are evident in each case (Figure **3**; Table **2**), and all redox potentials are reported relative to an external ferrocenium/ferrocene ($Fc^+$/Fc) standard. The cobalt(II) complex **2** provides a convenient starting point for interpretation of the voltammetric data. The cyclic and square-wave voltammograms (CV and SWV) of **2** exhibit quasireversible features at +0.84 and –1.34 V that are attributed to the $Co^{3+}/Co^{2+}$ and $Co^{2+}/Co^{1+}$ couples, respectively; these potentials are comparable values reported for $Co^{II}$ complexes with similar mixed N/P ligand sets.[13],[18] Furthermore, the closely-related dicobalt(II) complex, $[Co^{2+}_2(\mathbf{L^{N3O2}})(bpy)_2]^+$, displays cobalt-based oxidation and reduction events at +0.87 and –1.42 V, respectively.[9],[10] The third quasi-reversible feature at –0.31 V is then ascribed to one-electron oxidation of the μ-$NAr_2$ unit of the $\mathbf{L^{N3P2}}$ ligand. This assignment is consistent with literature reports of diarylamido-based pincer complexes, which generally exhibit a ligand-based oxidation between 0.32 and –0.34 V.[19]

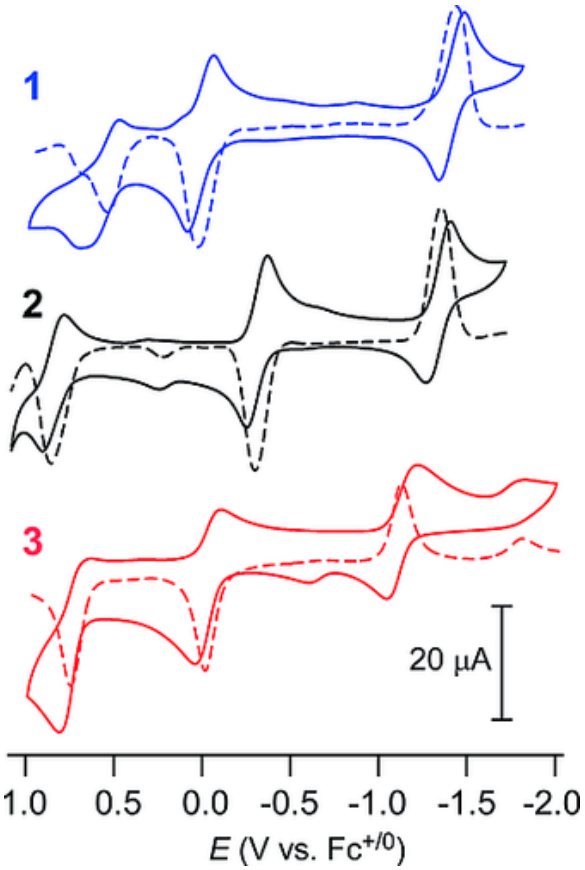

**Figure 3**. Cyclic voltammograms (solid lines) of complexes **1**–**3** (conc. = 2.0 mM) measured in $CH_2Cl_2$ with 0.1 M $(NBu_4)PF_6$ as the supporting electrolyte. Square-wave voltammograms measured under the same conditions are indicated by dashed lines. All scans rates were 100 mV/s.

**Table 2.** Summary of electrochemical data for complexes **1**–**3** in $CH_2Cl_2$.[a]Potentials reported in volts [V]

| Complex | $M^{3+/2+}$ ($\Delta E$) | $[L^{N3P2}]^{-/0}$ ($\Delta E$) | $M^{2+/1+}$ ($\Delta E$) |
|---|---|---|---|
| **1** | +0.53 (0.20) | +0.01 (0.14) | –1.42 (0.14) |
| **2** | +0.84 (0.13) | –0.31 (0.12) | –1.34 (0.14) |
| **3** | +0.71 (0.18) | –0.03 (0.14) | –1.14 (0.16) |

[a] All potentials are reported vs. the ferrocene/ferrocenium couple. $\Delta E = E_{p,a} - E_{p,c}$.

The voltammetric data collected for $[Fe^{2+}(L^{N3P2})]$OTf (**1**) exhibits a similar three event pattern (Figure **4**). On scanning to negative potentials a quasi-reversible cathodic process occurs at $E_{1/2}$= –1.42 V, corresponding to the $Fe^{2+}/Fe^{1+}$ couple. The wave near 0.0 V arises from oxidation of the $L^{N3P2}$ ligand, while the feature at +0.53 V is attributed to the $Fe^{3+}/Fe^{2+}$ couple. Similarly, the CV measured for $[Ni^{2+}(L^{N3P2})]$OTf (**3**) exhibits anodic peaks at –0.07 and +0.68 V that are assigned to $L^{N3P2}$- and $Ni^{II}$-based oxidations, respectively. The $Ni^{2+}/Ni^{+}$ couple is observed at –1.14 V. For the sake of comparison, a similar high-spin $Ni^{II}$ complex with mixed N/P ligation generated by Holm and co-workers features $Ni^{3+}/Ni^{2+}$ and $Ni^{2+}/Ni^{1+}$ couples at +0.55 and –0.85 V – comparable to the values observed for **3** (Table **2**).[20-22] Complex **3** also exhibits an irreversible cathodic peak at –1.81 V that is tentatively assigned to reduction of the $L^{N3P2}$ligand (vide infra).

The redox-active nature of the $L^{N3P2}$ ligand was further confirmed through spectroscopic and computational studies of $\mathbf{3}^{ox}$ – the one-electron oxidized derivative of **3**. Treatment of complex **3** with one equivalent of acetylferrocenium ($E_{1/2}$ = +0.27)[22] in $CH_2Cl_2$ yields the new chromophore $\mathbf{3}^{ox}$. The oxidized species is stable at room temperature, consistent with the quasireversibility of the redox couple observed at –0.03 V (Table **2**). The absorption spectrum of $\mathbf{3}^{ox}$ is dominated by a sharp, intense peak at 588 nm ($\varepsilon$ = 12000 $M^{-1}cm^{-1}$; Figure **4**) in addition to two broad bands with $\lambda_{max}$ = 740 and > 1100 nm. The corresponding X-band EPR spectrum, measured at 77 K in frozen $CH_2Cl_2$, reveals an axial $S$ = 1/2 signal with $g$-values of 2.04 and 2.01 (Figure **4**, inset). It is significant that the spectral features of $\mathbf{3}^{ox}$ closely resemble those observed upon one-electron oxidation of $[Ni^{2+}Cl(L^{PNP})]$ (**4**), where $L^{PNP}$ is a PNP-type pincer monanionic ligand featuring two $-P(iPr)_2$ substituents. As reported by Mindiola and co-workers, the absorption spectrum of $[NiCl(L^{PNP})]^+$ ($\mathbf{4}^{ox}$) features a sharp peak at 589 nm and a broader feature at 872 nm, similar to the pattern found for $\mathbf{3}^{ox}$.[23] Furthermore, the solid-state EPR spectrum of $\mathbf{4}^{ox}$ revealed a $S$ = 1/2 species with three resonances at $g$ = 2.040, 2.016, and 2.005. Detailed experimental and computational analysis determined that $\mathbf{4}^{ox}$ consists of a low-spin $Ni^{II}$ center bound to a $L^{PNP}$-based radical.

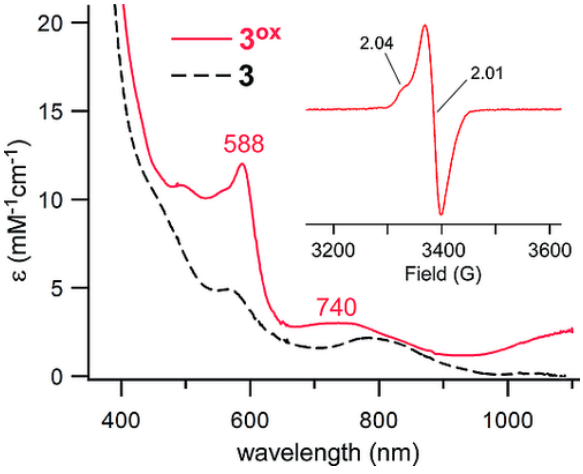

**Figure 4** UV/Vis absorption spectra of **3** (black dashed line) and **3$^{ox}$** (red solid line) measured in $CH_2Cl_2$ at room temperature. *Inset*: EPR spectrum of **3$^{ox}$**collected at 77 K in frozen $CH_2Cl_2$. Frequency = 9.497 GHz.

Given its $S$ = 1/2 ground state, there are three possible electronic configurations for **3$^{ox}$**: (i) low-spin Ni$^{III}$ bound to a closed-shell **L$^{N3P2}$** anion, (ii) high-spin Ni$^{II}$ antiferromagnetically coupled to a **L$^{N3P2}$**-based radical, or (iii) low-spin Ni$^{II}$ bound to a **L$^{N3P2}$**-based radical. The presence of a Ni$^{III}$ center is not consistent with the small g-anisotropy ($\Delta g = g_1 - g_3$) of ≈ 0.04 observed in the EPR spectrum, as true Ni$^{III}$ complexes generally exhibit $\Delta g$-values greater than 0.20.[24] In addition, DFT calculations of **3$^{ox}$** determined that the lowest-energy model (**3$^{ox}$-LS**) consists of a low-spin Ni$^{II}$ center bound to a **L$^{N3P2}$**-based radical. The $g$-values computed for **3$^{ox}$-LS** (2.031, 2.015, and 2.009) nicely match the experimental data.

The singly-occupied MO (SOMO) of **3$^{ox}$-LS** is primarily localized on the **L$^{N3P2}$** scaffold, as indicated by the orbital plot provided in Figure **5**. The largest portion of Mulliken spin density (50 %) is found on the diarylamido portion of the ligand in N1- and C-based p-orbitals oriented perpendicular to the aromatic rings. The amido N1 $2p_x$ orbital engages in a π-interaction with the Ni($d_{x^2-y^2}$) orbital, which allows a small amount (20 %) of unpaired spin to delocalize onto the metal center. The presence of partial metal character accounts for the modest shifts in the [**L$^{N3P2}$**]$^{-/0}$ couple across the **1**–**3** series, as observed experimentally (Table **2**). The remainder of the unpaired spin density in the SOMO resides on the imino (13 %) and phosphine (10 %) moieties.

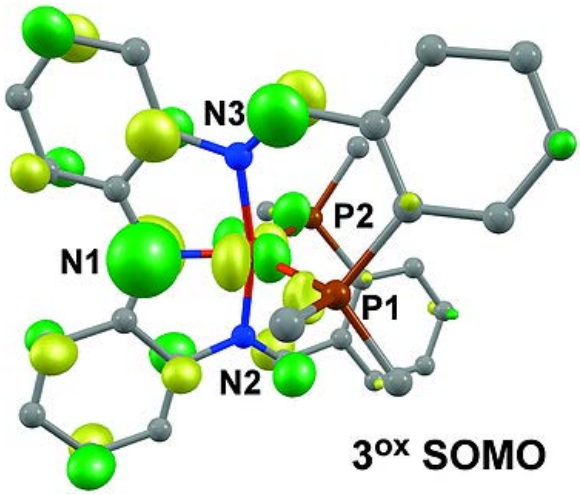


**Figure 5** Isosurface plots of the singly-occupied MO of **3$^{ox}$** generated from DFT calculations (BP86 functional). Hydrogen atoms are omitted for clarity.

Insights into the absorption features of **3$^{ox}$** were gained through time-dependent DFT (TD-DFT) computations that employed the range-separated cam-B3LYP hybrid functional. As shown in Figure S4, the TD-DFT methodology adequately reproduces the energies and intensities of the experimental absorption features. The calculations predict three intense transitions at 735, 610, and 465 nm. The identities of the computed transitions are revealed by electron density different maps (EDDMs), as provided in Figure S5. The lower-energy bands at 730 and 610 nm ($\varepsilon$ ≈ 5000 $M^{-1}cm^{-1}$) arise from Ni$^{II}$→**L$^{N3P2}$**-radical charge transfer (CT) transitions in which the acceptor orbital is the SOMO of **3$^{ox}$**. The more intense higher-energy feature at 465 nm ($\varepsilon$ = 15000 $M^{-1}cm^{-1}$) has contributions from two overlapping **L$^{N3P2}$**-based π-radical transitions, which also possess a small degree of metal-to-ligand CT (MLCT) character. Based on the TD-DFT results, we assign the strong experimental absorption peak at 588 nm ($\varepsilon$ = 12000 $M^{-1}cm^{-1}$) to a π-radical transition, while the two weaker bands with $\lambda_{max}$ > 700 nm are attributed to MLCT transitions.

## Electrocatalytic Proton Reduction

To probe the catalytic ability of complex **2**, we evaluated its electrochemical behavior in anhydrous MeCN and in the presence of acetic acid. This acid seemingly leads to deactivation of the catalyst, as evidenced by UV/Visible spectroscopy. However, mild catalytic activity was observed in the presence of multiple equivalents of 4-*tert*-butylphenol as the proton source. This substrate exhibits a p$K_a$ of 27.5 in MeCN, thus being a weaker proton source than acetic acid (p$K_a$ = 22.3 in MeCN). The CV data shown in Figure **6**(a) revealed catalytic peaks appearing at fairly negative potentials below –2.0 V vs. $Fc/Fc^+$. The peaks increase with an increasing amount of acid, thus associating this process with catalytic dihydrogen generation. Control experiments were carried out in the absence of **2** and no catalytic peak was observed, therefore confirming that the presence of the complex is required for catalysis (Figure S6).

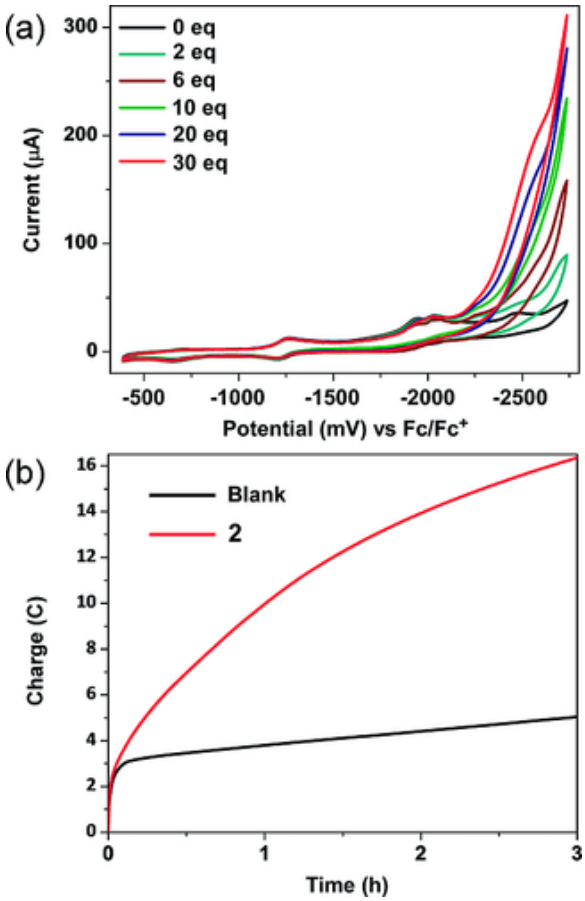


**Figure 6** (a) Cyclic voltammograms (CVs) of **2** (1 mM) measured vs. Ag/AgCl and plotted vs. $Fc/Fc^+$ in presence of increasing concentrations of 4-*tert*-butylphenol (0–30 equiv.) in 5 mL of MeCN and 0.1 M $TBAPF_6$ as supporting electrolyte. Glassy carbon and Pt wire are respectively the working and auxiliary electrodes. (b) Charge consumption vs. time during bulk electrolysis. Conditions: $TBAPF_6$ (1.56 g); 4-*tert*-butylphenol (0.07 g, 0.5 mmol); catalyst (4.64 mg, 0.005 mmol) and MeCN (20 mL) at an applied potential of –2000 mV (vs. Ag/AgCl).

A bulk electrolysis experiment was performed to quantify the amount of dihydrogen generated. A three-electrode set up was used with mercury pool as the working electrode and an applied potential of –2000 $mV_{Ag/AgCl}$ in MeCN with 100 equivalents of acid. The charge vs. time plot is shown in Figure **7**(b). The non-linear behavior indicates the instability of the catalyst under these conditions. After 3 h of catalysis a turnover number (TON) of 6 was detected with a Faradaic efficiency (FE) of 77 %. These results are the average of at least three measurements and suggest that complex **2** is moderately catalytic for proton reduction with an approximate proton consumption of circa 10 %. Other cobalt catalysts in planar oxime platforms have shown TONs of 10–18

under similar conditions[25] while a phenolate-rich catalyst has shown TON of 10.8.[9] Considerably higher TONs have been observed for pyridine-rich platforms with cobalt (15.4).[26]

UV/Visible spectral changes were analyzed before and after catalysis in order to shed light on catalyst deactivation, and the resulting spectra are provided in Figure S7. The intense peak at 493 nm experiences a red-shift to ca. 540 nm during catalysis and its intensity decreases. The band at 800 nm is also diminished. The loss of absorption intensity for these charge-transfer and ligand-based bands (vide supra) suggests that the $\mathbf{L}^{N3P2}$ framework is degraded at the low-potentials used in the electrocatalytic experiments.

Based on the electrochemical data presented in Figure **7**, it is evident that the cobalt complex (**2**) requires reduction by two electrons in order to initiate electrocatalysis with weakly acidic proton sources like 4-*tert*-butylphenol. The doubly-reduced species formally possesses a $Co^0$center, although the possibility of $\mathbf{L}^{N3P2}$-based reduction must also be considered. We therefore employed DFT geometry optimizations to generate computational models of the singly- and doubly-reduced derivatives of the cobalt complex ($\mathbf{2}^{red1}$ and $\mathbf{2}^{red2}$, respectively). The electronic structure of neutral $\mathbf{2}^{red1}$ is consistent with a low-spin $Co^I$ center possessing a $\{d_{xy}^2\ d_{xz}^2\ d_{yz}^2\ d_{x^2-y^2}^2\ d_{z^2}^0\}$ configuration. The high-spin ($S$ = 1) $\mathbf{2}^{red1}$ model is higher in energy by 6.4 kcal/mol. Thus, DFT predicts that the initial reduction of **2** is metal-based, consistent with our prior analysis of the CV data (vide supra).

For the second reduction, the electron could be added either to the empty $Co(d_{z^2})$-based MO or the LUMO of the $\mathbf{L}^{N3P2}$ ligand. DFT calculations favor the latter possibility, as the lowest-energy $\mathbf{2}^{red2}$ model features a low-spin $Co^I$ center bound to a $\mathbf{L}^{N3P2}$ dianion radical. The corresponding $S$ = 3/2 model, which also contains a $\mathbf{L}^{N3P2}$-based radical, is higher in energy by 2.1 kcal/mol. The unpaired spin density in low-spin $\mathbf{2}^{red2}$ is largely concentrated on the two iminyl moieties (64 %) with partial delocalization onto the aryl phosphine rings (Figure S8). Reduction of the $\mathbf{L}^{N3P2}$ ligand is futher reflected in the elongation of the imine N–C bonds by 0.026 Å upon conversion of low-spin $\mathbf{2}^{red1}$ to $\mathbf{2}^{red2}$, combined with a 0.021 Å contraction in the adjacent C–C bond (Table S2). In addition, there is little difference in axial Co–N2/N3 bond lengths between $\mathbf{2}^{red1}$ and $\mathbf{2}^{red2}$, indicating that the $Co(d_{z^2})$-based MO remains unoccupied. These computational results suggest that the $\mathbf{L}^{N3P2}$ ligand exists as a dianion radical in the catalytically-active species ($\mathbf{2}^{red2}$). The reduction of the $\mathbf{L}^{N3P2}$ ligand may contribute to the instability of **2** under catalytic conditions, as described above.

## 3. Conclusions

In this manuscript we have investigated the coordination chemistry and non-innocent redox behavior of a novel pentadentate diarylamido-based ligand. Whereas the related $\mathbf{L}^{N3O2}$ ligand (Scheme **2**) was previously shown to support bimetallic structures,[9] the greater length of aryl C–P bonds allows all five donors of the $\mathbf{L}^{N3P2}$ chelate to bind to the same metal ion without excessive strain. X-ray crystal structures of the resulting Fe (**1**), Co (**2**), and Ni (**3**) complexes revealed nearly identical trigonal-bipyramidal geometries (Figure **7**). Structural, magnetic, and computational results indicate that all three complexes are low-spin in the solid state. The Fe and Co complexes remain low-spin in solution, while $^1$H NMR studies found that the Ni complex converts to the high-spin state.

The $\mathbf{L}^{N3P2}$-based complexes exhibit three quasi-reversible redox couples between +1.0 and –1.5 V vs. $Fc^+$/Fc in $CH_2Cl_2$ (Table **2**; Figure **7**). The events at high and low potentials correspond to oxidation and reduction, respectively, of the $M^{II}$ centers, while the intermediate event is due to oxidation of the $\mathbf{L}^{N3P2}$ ligand. Consistent with prior electrochemical studies of diarylamido pincer complexes, the $\mathbf{L}^{N3P2}$-based oxidations are observed at potentials near 0.0 V.[19] Further insights into the redox activity of the $\mathbf{L}^{N3P2}$ ligand were gained through chemical oxidation of the nickel complex (**3**), which afforded the relatively stable species $\mathbf{3}^{ox}$. The EPR and UV/Vis absorption features of $\mathbf{3}^{ox}$ are typical of complexes with diarylaminyl radicals.[23] By interpreting the spectroscopic

data with the aid of DFT calculations, we concluded that **3**$^{ox}$consists of a low-spin Ni$^{II}$ center bound a **L**$^{N3P2}$-based radical.

The electrocatalytic properties of **2** were surveyed in the presence of weak acids. Initial experiments with acetic acid resulted in catalyst decomposition, necessitating the use of 4-*tert*-butylphenol as the proton source. Modest catalytic activity at potentials below –2.0 V in MeCN was observed with a Faradaic efficiency (FE) of 77 %. Electronic structure calculations indicate that the catalytically-competent cobalt species (**2**$^{red2}$) features a reduced **L**$^{N3P2}$ ligand and Co$^{I}$center. The loci of the ligand-based reduction are the two iminyl groups that link the diarylamide to the aryl phosphine donors. In this way, the mechanism employed by **2** resembles those found for HER and $CO_2$ reduction electrocatalysts with redox-active bpy,[27] α-diimine,[28] and 2,6-bis(imino)pyridine ligands.[13], [13], [29]

Even though the catalytic performance of **2** is limited by its instability under the rugged conditions employed in the bulk electrolysis experiments, our results suggest possible modifications to the **L**$^{N3P2}$ framework that are likely to improve catalyst performance and stability. For instance, replacement of the central diarylamido unit with a 4,5-disubstituted acridine (or phenazine) donor would yield a neutral N3P2-chelate, making it easier to reduce both the Co$^{II}$ center and ligand. This arrangement would have the added advantage of facilitating charge delocalization from the imine moieties to the central N1-donor, thereby stabilizing the ligand-reduced complex. Attaching methyl substituents to the imine donors, as found in the redox-active 2,6-bis(imino)pyridine ligands, may also slow degradation of the catalyst at low potentials. Efforts are currently underway to determine whether these ligand changes yield more robust electrocatalysts for multielectron transformations.

## Experimental Section

**Materials and Physical Methods:** Reagents and solvents were purchased from commercial sources and used as received, unless otherwise noted. Dichloromethane ($CH_2Cl_2$) was purified and dried using a Vacuum Atmospheres solvent purification system and stored under $N_2$. The synthesis and handling of complexes **1**–**3** were carried out in a Vacuum Atmospheres Omni-Lab glovebox under inert atmosphere. The compound 2-(diphenylphosphanyl)benzaldehyde was prepared according to published procedures.[14], [30]

UV/Vis absorption spectra were collected with an Agilent 8453 diode array spectrometer, and infrared (IR) spectra were measured using a Nicolet Magna-IR 560 spectrometer. X-band EPR spectra were obtained with a Bruker EMXplus instrument equipped with an ER4416DM cavity, an Oxford Instruments ESR900 helium flow cryostat, and Oxford Instruments ITC503 temperature controller. Simulations of the experimental EPR spectra were performed using the program *EasySpin* (version 5).[31] Solid-state magnetic measurements were performed at room temperature using an AUTO balance manufactured by Sherwood Scientific. $^1$H NMR spectra were recorded on a Varian 400 MHz spectrometer. Elemental analyses were performed at Midwest Microlab, LLC in Indianapolis, IN. Cyclic and square-wave voltammograms were measured under inert atmosphere with an epsilon EC potentiostat (iBAS) at a scan rate of 100 mV/s with 0.1 M $[NBu_4]PF_6$ electrolyte. The three-electrode cell consisted of a Ag/AgCl reference electrode, a platinum auxiliary electrode, and a glassy carbon working electrode. Under these conditions, the ferrocene/ferrocenium ($Fc^{+/0}$) couple has an $E_{1/2}$ value of +0.51 V in $CH_2Cl_2$.

**Synthesis of Pro-Ligand HL$^{N3P2}$:** Bis(2-amino-4-methylphenyl)amine[10] (227 mg, 1.0 mmol, 1 equiv.), 2-(diphenylphosphanyl)benzaldehyde (580 mg, 2.0 mmol, 2 equiv.), molecular sieves (4 Å), and toluene (30 mL) were added to a 100 mL round-bottom flask equipped with a stir bar. The mixture was stirred overnight at 90 °C under nitrogen atmosphere, during which time the solution turned to a deep red color. Once the reaction had reached completion (as determined by TLC), the solution was cooled to room temperature and filtered to remove the molecular sieves. Evaporation of the solvent under vacuum provided a deep red residue. The crude solid was then dissolved in diethyl ether (5 mL), filtered, and dried *en vacuo* to yield the desired product as a

dark red powder (632 mg, 0.83 mmol, 83 % yield). This material was used for metalation reactions without further purification. UV/Vis ($CH_2Cl_2$): $\lambda_{max}$ ($\varepsilon$, $M^{-1}$ $cm^{-1}$) = 322 (sh), 431 nm (4600). IR (solid): $\tilde{\nu}$ = 3048 (w), 2903 (w), 2854 (w), 1695 (m), 1599 (m), 1507 (s), 1431 (s), 1309 (m), 1256 (m), 1197 (m) $cm^{-1}$. $^1$H NMR ($CD_2Cl_2$): $\delta$ = 2.23 (s, 6 H), 6.40 (s, 2 H), 6.95 (d, 4 H), 7.11–7.17 (m, 4 H), 7.30–7.43 (m, 22 H), 7.80 (s, 1 H), 8.30 (s, 2 H), 9.16 (d, 2 H) ppm. $^{13}$C NMR ($CD_2Cl_2$): $\delta$ = 20.9, 115.2, 118.8, 128.2, 128.3, 128.4, 129.2, 129.3, 129.4, 129.6, 129.7, 131.2, 133.9, 134.6, 134.8, 136.0, 136.9, 137.0, 139.1, 139.4, 139.7, 139.8, 140.0, 156.7, 157.0 ppm. $^{31}$P NMR ($CD_2Cl_2$): $\delta$ = –13.45 ppm.

**General Procedure for Synthesis of Complexes 1–3:** In a 25 mL round-bottom flask, the pro-ligand H**L**$^{N3P2}$ (154 mg, 0.20 mmol) was dissolved in a 1:1 mixture of MeCN/$CH_2Cl_2$ (10 mL), followed by addition of an equimolar amount of the appropriate $M^{II}$ salt: $Fe(OTf)_2$ (**1**), $Co(ClO_4)_2{\cdot}6H_2O$ (**2**), or $Ni(ClO_4)_2{\cdot}6H_2O$ (**3**). The mixture was stirred for 5 min. Subsequent addition of one equivalent of base (either $NEt_3$ or NaOMe) caused the solution to turn to a deep brown color. The mixture was stirred overnight, filtered through Celite, and the solvent removed under vacuum. The resulting powder was washed with pentane (5 mL) and dried under vacuum to yield analytically-pure material. Crystals suitable for crystallographic experiments were obtained in the manner described below for each complex.

**[Fe(L$^{N3P2}$)]OTf (1):** Yield: 152 mg, 78 %. Crystals suitable for crystallographic analysis were grown by vapor diffusion of diethyl ether into a concentrated 1,2-dichloroethane solution. The resulting X-ray structure revealed 1.3 equiv. of triflate anion per Fe center (Table S1). $C_{53.3}H_{42}F_{3.9}FeN_3O_{3.9}P_2S_{1.3}$ (MW = 975.77 g $mol^{-1}$): calcd. C 62.73, H 4.15, N 4.12; found C 63.13, H 4.57, N, 4.21. UV/Vis ($CH_2Cl_2$): $\lambda_{max}$ ($\varepsilon$, $M^{-1}$ $cm^{-1}$) = 446 (17200), 570 (10570), 793 nm (8340). IR (solid): $\tilde{\nu}$ = 3052 (w), 2916 (w), 2854 (w), 1696 (w), 1672 (w), 1599 (w), 1583 (w), 1513 (m), 1490 (m), 1432 (s), 1394 (m), 1350 (w), 1309 (m), 1258 (s), 1236 (s), 1220 (s), 1147 (s) $cm^{-1}$. $^1$H NMR ($CD_2Cl_2$): $\delta$ = 2.32 (s, 6 H), 6.56 (t, 4 H), 6.89–6.98 (m, 4 H), 7.03 (t, 4 H), 7.10–7.20 (m, 6 H), 7.24–7.33 (m, 6 H), 7.50–7.56 (m, 4 H), 7.68–7.80 (m, 6 H), 9.56 (s, 2 H) ppm. $^{31}$P NMR ($CD_2Cl_2$): $\delta$ = 84.85 ppm.

**[Co(L$^{N3P2}$)]$ClO_4$ (2):** Yield: 136 mg, 73 %. Slow evaporation of a concentrated $CH_2Cl_2$ solution of the crude product provided deep red-brown crystals that were collected by filtration. Single crystals of **2** suitable for X-ray diffraction experiments were grown from a concentrated 1:1 $CH_2Cl_2$/MeCN solution. $C_{52}H_{42}ClCoN_3O_4P_2$ (MW = 929.24 g $mol^{-1}$): calcd. C 67.21, H 4.56, N 4.52; found C 66.98, H 4.48, N 4.39. UV/Vis ($CH_2Cl_2$): $\lambda_{max}$ ($\varepsilon$, $M^{-1}$ $cm^{-1}$) = 362 (sh), 493 (21600), 798 nm (5900). IR (solid): $\tilde{\nu}$ = 3050 (w), 2913 (w), 2856 (w), 1694 (w), 1670 (w), 1604 (w), 1583 (w), 1521 (w), 1488 (m), 1433 (m), 1358 (m), 1286 (m), 1239 (m), 1161 (m) $cm^{-1}$. $\mu_{eff}$ = 1.71 $\mu_B$ (Evans method).

**[Ni(L$^{N3P2}$)]$ClO_4$ (3):** Yield: 115 mg, 62 %. Slow evaporation of a concentrated $CH_2Cl_2$ solution of the crude product provided deep brown crystals that were collected by filtration. Single crystals of **3** suitable for X-ray diffraction experiments were grown from a concentrated 1:1 $CH_2Cl_2$/MeCN solution. $C_{52}H_{42}ClNiN_3O_4P_2$ (MW = 929.00 g $mol^{-1}$): calcd. C 67.23, H 4.56, N 4.52; found C 66.89, H 4.40, N 4.26. UV/Vis ($CH_2Cl_2$): $\lambda_{max}$ ($\varepsilon$, $M^{-1}$ $cm^{-1}$) = 444 (11330), 572 (4880), 801 nm (2160). IR (solid): $\tilde{\nu}$ = 3051 (w), 2908 (w), 2852 (w), 1693 (m), 1671 (w), 1601 (w), 1583 (w), 1515 (w), 1493 (s), 1433 (s), 1363 (m), 1285 (m), 1237 (s), 1157 (m) $cm^{-1}$. $^1$H NMR ($CD_2Cl_2$): $\delta$ = –76.6 (2 H), –8.2 (4 H), –5.1 (4 H), 7.3 (12 H), 12.0 (2 H), 15.0 (4 H), 18.1 (4 H), 32.6 (2 H), 56.8 (2 H), 90.5 (6 H) ppm. $^{31}$P NMR ($CD_2Cl_2$): $\delta$ = 35.27. $\mu_{eff}$ = 2.80 $\mu_B$ (Evans method).

**X-ray Crystallography:** X-ray crystal structures were obtained with an Oxford Diffraction SuperNova kappa-diffractometer (Rigaku Corp.) equipped with dual Cu/Mo X-ray sources, X-ray mirror optics, an Atlas CCD detector, and a low-temperature Cryojet device. The data were processed with the CrysAlis Pro program package, followed by numerical absorption correction based on Gaussian integration over a multifaceted crystal model. The empirical absorption correction, using spherical harmonics, was implemented in the SCALE3 ABSPACK scaling algorithm. Structures were solved using the SHELXS program and refined with the SHELXL

program[32] as part of the Olex2 crystallographic package.[33] X-ray diffraction parameters are summarized in Table S1. The crystallographic data (CIF) obtained from the Cambridge Crystallographic Data Centre (**www.ccdc.cam.ac.uk/data_request/cif**) using the deposition numbers 1819809 (**1**), 1819810 (**2**), and 1819811 (**3**). To examine the possibility that the $Ni^{II}$ center of **3** undergoes a spin transition in the solid state at elevated temperatures, crystallographic data were also collected at 240 K (CCDC 1819812). As shown in Table S3, the axial Ni–N2/N3 bonds in the 240 K structure are slightly elongated by 0.039(3) Å relative to the 100 K structure, whereas the equatorial Ni–N1 and Ni–P1/P2 bonds are virtually unchanged. Such minor changes in metric parameters between the 100 and 240 K structures indicate that the $Ni^{II}$ center in **3** is predominantly low-spin throughout this temperature range.

**CCDC** 1819809 (for **1**), 1819810 (for **2**), 1819811 (for **3**), and 1819812 (for **3** at 240 K) contain the supplementary crystallographic data for this paper. These data can be obtained free of charge from **The Cambridge Crystallographic Data Centre**.

**Computational Methods:** Density functional theory (DFT) calculations were performed using the ORCA 3.0 software package developed by Dr. F. Neese (MPI for Chemical Energy Conversion).[34] Using the X-ray crystal structures as starting points, computational models of complexes **1**–**3** were generated via unrestrained geometry optimizations. The $\mathbf{L^{N3P2}}$ ligand was truncated by replacing the phenyl substituents of the phosphine donors with methyl groups. The presence of only real vibrational frequencies in the numerical frequency calculations confirmed that all structures corresponded to a local energy minima. Zero-point energies, thermal corrections, and entropy terms were obtained from these frequency calculations. Geometry optimizations of complexes **1**–**3** employed either the non-hybrid Becke–Perdew (BP86) functional[35] or Becke's three-parameter hybrid functional for exchange along with the Lee–Yang–Parr correlation functional (B3LYP).[36] The BP86 method offered better agreement with the crystallographic data (Tables S4–S6); therefore, calculations of oxidized and reduced species (e.g., $\mathbf{3^{ox}}$, $\mathbf{2^{red1}}$, $\mathbf{2^{red2}}$) were carried out using this functional. All calculations employed the spin-unrestricted formalism and utilized Ahlrichs' valence triple-ζ basis set (TZV) and TZV/J auxiliary basis set, in addition to polarization functions on main-group and transition-metal elements (default-basis 3 in ORCA).[37] The presence of solvent was simulated with the conductor-like screening model (COSMO; dielectric constant of 9.08 for $CH_2Cl_2$).[38] Cartesian coordinates for selected computational models are provided in the Supplementary Information (Tables S7–S9).

EPR parameters (**g-** and **A**-tensors) were computed by solving the coupled-perturbed self-consistent field (CP-SCF) equations[39] to determine spin-orbit coupling contributions. EPR calculations utilized the “core properties” with extended polarization [CP(PPP)] basis set[40] for transition metal atoms and Kutzelnigg's NMR/EPR (IGLO-III) basis set[41] for first-sphere atoms (N and P). A high resolution grid with an integration accuracy of 7.0 was applied to the metal center, phosphorus, and nitrogen atoms. Time-dependent DFT (TD-DFT) calculations employed the cam-B3LYP range-separated hybrid functional,[42] which has proven reliable in previous studies.[43] Absorption energies and intensities were computed for 40 excited states with the Tamm-Dancoff approximation.[44] Isosurface plots of molecular orbitals were prepared using the *ChemCraft* program.

**Electrochemistry and Bulk Electrolysis:** The electrochemical behavior of complex **2** was investigated with a BAS 50W potentiostat/galvanostat. Cyclic voltammograms were obtained at room temperature in $CH_3CN$ solutions containing 0.1 M of $n Bu_4NPF_6$ as the supporting electrolyte under an argon atmosphere. The electrochemical cell was comprised of three electrodes: glassy-carbon (working), platinum wire (auxiliary) and Ag/AgCl (reference). The ferrocene/ferrocenium redox couple $Fc/Fc^+$ ($E°$ = 400 mV vs. NHE)[45] was used as the internal standard. Peak to peak potential separation ($\Delta E_p = |E_{p,c} - E_{p,a}|$) and $|i_{pa}/i_{pc}|$ values were measured to evaluate the reversibility of the redox processes. Bulk electrolysis was performed in a custom-made air-tight H-type cell with vitreous carbon as the working electrode, Ag/AgCl as the reference electrode placed in the same compartment and a Pt-coil used as the auxiliary electrode placed in another compartment separated by a frit. Controlled potential

electrolysis of the complex has been done in 20 mL of $CH_3CN$ with tetrabutyl ammonium hexafluorophosphate ($TBAPF_6$) as supporting electrolyte until the calculated final charge is attained. Potentials were applied to the cell by a BAS 50W potentiostat/galvanostat and measured against the Ag/AgCl reference electrode.

**Catalytic Activity:** Proton reduction electrocatalysis was evaluated for by cyclic voltammetry in presence of 4-tertbutyl phenol using glassy carbon as working electrode, platinum wire as auxillary and Ag/AgCl as reference electrodes with tetra-butyl ammonium hexafluorophosphate($TBAPF_6$) as supporting electrolyte. To determine the amount of dihydrogen release, bulk electrolysis has been performed in a custom-made air-tight H-type cell in the presence of mercury-pool as working electrode, Ag/AgCl as reference electrode placed in the same compartment whereas Pt-coil used as the auxiliary electrode placed in the other compartment separated by a frit. $TBABF_4$ was used as the supporting electrolyte. The main chamber was filled with an electrolyte solution and proton source ($TBAPF_6$: 1.56 g; 4-tertbutyl phenol 0.075 g [4 mmol], 20 mL of $CH_3CN$) and the glass-fitted chamber was filled with another electrolyte solution ($TBAPF_6$: 0.39 g; 5 mL of $CH_3CN$). In a standard experiment, the cell was purged with $N_2$ gas for 20 min followed by sample head space gas (100 µL) to ensure $O_2$-free environment in the gas chromatograph (GC). The head space gas was again injected into the GC and the amount of dihydrogen was recorded. Faradaic efficiency was calculated from the gas chromatography measurements using the equation $\%FE = [(n_{H2})/(Q/2)] \times 100$, where $Q$ is in Faraday unit. The GC is a Gow-Mac 400 instrument equipped with a thermal conductivity detector. An 8′ X 1/8′′ long 5 Å molecular sieves column operating at 60 °C was used with the carrier gas $N_2$. The calibration was carried out with dihydrogen gas (Dihydrogen GC grade 99.99 %, Scotty analyzed gases, Sigma Aldrich).

## Acknowledgements

A. T. F. is grateful for financial support from the U.S. National Science Foundation (CHE-1056845), including funding to upgrade the X-band EPR instrument at Marquette University (CHE-1532168). C. N. V. acknowledges support from the National Science Foundation through grant NSF-CHE-1500201, as well as from the U.S. Department of Energy, Office of Science, Office of Basic Energy Sciences through grant DE-SC0001907. D. M. E. acknowledges support by the Thomas C. Rumble University Graduate Fellowship from Wayne State University.

## Supporting Information

| Filename | Description |
|---|---|
| ejic201800843-sup-0001-SupMat.pdf1.3 MB | Supporting Information |

Please note: The publisher is not responsible for the content or functionality of any supporting information supplied by the authors. Any queries (other than missing content) should be directed to the corresponding author for the article.

## References

1a) Benson, E. E., Kubiak, C. P., Sathrum, A. J. and Smieja, J. M., *Chem. Soc. Rev.*,2009, **38**, 89– 99; b) Appel, A. M., Bercaw, J. E., Bocarsly, A. B., Dobbek, H., DuBois, D. L., Dupuis, M.,Ferry, J. G., Fujita, E., Hille, R., Kenis, P. J. A., Kerfeld, C. A., Morris, R. H., Peden, C. H. F., Portis, A. R., Ragsdale, S. W., Rauchfuss, T. B., Reek, J. N. H., Seefeldt, L. C.,Thauer, R. K. and Waldrop, G. L., *Chem. Rev.*, 2013, **113**, 6621– 6658; c) Schneider, J., Jia, H., Muckerman, J. T. and Fujita, E., *Chem. Soc. Rev.*, 2012, **41**,2036– 2051; d) DuBois, D. L., *Inorg. Chem.*, 2014, **53**, 3935– 3960.

2a) Artero, V., Chavarot-Kerlidou, M. and Fontecave, M., *Angew. Chem. Int. Ed.*,2011, **50**, 7238– 7266; *Angew. Chem.*, 2011, **123**, 7376; b) Wang, M., Chen, L. and Sun, L., *Energy Environ. Sci.*, 2012, **5**, 6763– 6778; c) Du, P. and Eisenberg, R., *Energy Environ. Sci.*, 2012, **5**, 6012– 6021; d) Thoi, V. S., Sun, Y., Long, J. R. and Chang, C. J., *Chem. Soc. Rev.*, 2013, **42**, 2388– 2400; e) McKone, J. R., Marinescu, S.

C., Brunschwig, B. S., Winkler, J. R. and Gray, H. B., *Chem. Sci.*, 2014, **5**, 865– 878; f) Queyriaux, N., Jane, R. T., Massin, J., Artero, V. and Chavarot-Kerlidou, M., *Coord. Chem. Rev.*, 2015, **304–305**, 3– 19.

3a) Nippe, M., Khnayzer, R. S., Panetier, J. A., Zee, D. Z., Olaiya, B. S., Head-Gordon, M., Chang, C. J., Castellano, F. N. and Long, J. R., *Chem. Sci.*, 2013, **4**,3934– 3945; b) Luca, O. R. and Crabtree, R. H., *Chem. Soc. Rev.*, 2013, **42**, 1440– 1459; c) Lyaskovskyy, V. and Bruin, B., *ACS Catal.*, 2012, **2**, 270– 279.

4a) Dempsey, J. L., Brunschwig, B. S., Winkler, J. R. and Gray, H. B., *Acc. Chem. Res.*, 2009, **42**, 1995– 2004; b) Kaeffer, N., Chavarot-Kerlidou, M. and Artero, V., *Acc. Chem. Res.*, 2015, **48**,1286– 1295.

5 Zhao, X., Wang, P. and Long, M., *Comments Inorg. Chem.*, 2017, **37**, 238– 270.

6a) Khnayzer, R. S., Thoi, V. S., Nippe, M., King, A. E., Jurss, J. W., El Roz, K. A.,Long, J. R., Chang, C. J. and Castellano, F. N., *Energy Environ. Sci.*, 2014, **7**, 1477– 1488; b) Zee, D. Z., Chantarojsiri, T., Long, J. R. and Chang, C. J., *Acc. Chem. Res.*, 2015,**48**, 2027– 2036.

7a) McCrory, C. C. L., Uyeda, C. and Peters, J. C., *J. Am. Chem. Soc.*, 2012, **134**,3164– 3170; b) Gimbert-Surinach, C., Albero, J., Stoll, T., Fortage, J., Collomb, M.-N., Deronzier, A., Palomares, E. and Llobet, A., *J. Am. Chem. Soc.*, 2014, **136**, 7655– 7661; c) Moonshiram, D., Gimbert-Surinach, C., Guda, A., Picon, A., Lehmann, C. S.,Zhang, X., Doumy, G., March, A. M., Benet-Buchholz, J., Soldatov, A., Llobet, A.and Southworth, S. H., *J. Am. Chem. Soc.*, 2016, **138**, 10586– 10596.

8 Hogue, R. W., Schott, O., Hanan, G. S. and Brooker, S., *Chem. Eur. J.*, 2018, **24**,9820– 9832.

9a) Basu, D., Allard, M. M., Xavier, F. R., Heeg, M. J., Schlegel, H. B. and Verani, C. N., *Dalton Trans.*, 2015, **44**, 3454– 3466; b) Kpogo, K. K., Mazumder, S., Wang, D., Schlegel, H. B., Fiedler, A. T. and Verani, C. N., *Chem. Eur. J.*, 2017, **23**, 9272– 9279.

10 Wang, D., Lindeman, S. V. and Fiedler, A. T., *Inorg. Chem.*, 2015, **54**, 8744– 8754.

11a) Liang, L.-C., *Coord. Chem. Rev.*, 2006, **250**, 1152– 1177; b) Ozerov, O. V., in: *The Chemistry of Pincer Complexes* (Eds.: D. Morales-Moralesand C. M. Jensen), Elsevier, Amsterdam, 2007, pp. 287– 310.

12a) Trovitch, R. J., *Acc. Chem. Res.*, 2017, **50**, 2842– 2852; b) Mukhopadhyay, T. K., Rock, C. L., Hong, M., Ashley, D. C., Groy, T. L., Baik, M.-H. and Trovitch, R. J., *J. Am. Chem. Soc.*, 2017, **139**, 4901– 4915; c) Pal, R., Cherry, B. R., Flores, M., Groy, T. L. and Trovitch, R. J., *Dalton Trans.*,2016, **45**, 10024– 10033; d) Mukhopadhyay, T. K., Flores, M., Groy, T. L. and Trovitch, R. J., *J. Am. Chem. Soc.*,2014, **136**, 882– 885; e) Ben-Daat, H., Hall, G. B., Groy, T. L. and Trovitch, R. J., *Eur. J. Inorg. Chem.*, 2013,**2013**, 4430– 4442.

13a) Wiedner, E. S., Yang, J. Y., Dougherty, W. G., Kassel, W. S., Bullock, R. M.,DuBois, M. R. and DuBois, D. L., *Organometallics*, 2010, **29**, 5390– 5401; b) Tatematsu, R., Inomata, T., Ozawa, T. and Masuda, H., *Angew. Chem. Int. Ed.*,2016, **55**, 5247– 5250; *Angew. Chem.*, 2016, **128**, 5333; c) Rao, G. K., Pell, W., Gabidullin, B., Korobkov, I. and Richeson, D., *Chem. Eur. J.*,2017, **23**, 16763– 16767; d) Mukhopadhyay, T. K., MacLean, N. L., Gan, L., Ashley, D. C., Groy, T. L., Baik, M.-H., Jones, A. K. and Trovitch, R. J., *Inorg. Chem.*, 2015, **54**, 4475– 4482; e) Mukhopadhyay, T. K., MacLean, N. L., Flores, M., Groy, T. L. and Trovitch, R. J., *Inorg. Chem.*, 2018, **57**, 000– 000; f) Pal, R., Laureanti, J. A., Groy, T. L., Jones, A. K. and Trovitch, R. J., *Chem. Commun.*, 2016, **52**, 11555– 11558.

14a) Jarvis, A. G., Sehnal, P. E., Bajwa, S. E., Whitwood, A. C., Zhang, X., Cheung, M. S., Lin, Z. and Fairlamb, I. J. S., *Chem. Eur. J.*, 2013, **19**, 6034– 6043; b) Jarvis, A. G., Whitwood, A. C. and Fairlamb, I. J. S., *Dalton Trans.*, 2011, **40**,3695– 3702.

15a) Carabineiro, S. A., Bellabarba, R. M., Gomes, P. T., Pascu, S. I., Veiros, L. F.,Freire, C., Pereira, L. C. J., Henriques, R. T., Oliveira, M. C. and Warren, J. E., *Inorg. Chem.*, 2008, **47**, 8896– 8911; b) Dapporto, P. and Fallani, G., *J. Chem. Soc., Dalton Trans.*, 1972, 1498– 1501; c) Zell, T., Langer, R., Iron, M. A., Konstantinovski, L., Shimon, L. J. W., Diskin-Posner, Y., Leitus, G., Balaraman, E., Ben-David, Y. and Milstein, D., *Inorg. Chem.*,2013, **52**, 9636– 9649; d) Peng, D., Zhang, Y., Du, X., Zhang, L., Leng, X., Walter, M. D. and Huang, Z., *J. Am. Chem. Soc.*, 2013, **135**, 19154– 19166; e) Ma, H., Petersen, J. L., Young, V. G., Yee, G. T. and Jensen, M. P., *J. Am. Chem. Soc.*, 2011, **133**, 5644– 5647; f) Speiser, F., Braunstein, P. and Saussine, L., *Dalton Trans.*, 2004, 1539– 1545.

16 Evans, D. F., *J. Chem. Soc.*, 1959, 2003– 2005.

17a) Stelzer, O., Sheldrick, W. S. and Subramanian, J., *J. Chem. Soc., Dalton Trans.*,1977, 966– 970; b) Jenkins, D. M., Bilio, A. J. D., Allen, M. J., Betley, T. A. and Peters, J. C., *J. Am. Chem. Soc.*, 2002, **124**, 15336– 15350.

18a) Santra, B. K. and Lahiri, G. K., *J. Chem. Soc., Dalton Trans.*, 1998, 139– 146; b) Jacobsen, G. M., Yang, J. Y., Twamley, B., Wilson, A. D., Bullock, R. M., DuBois, M. R. and DuBois, D. L., *Energy Environ. Sci.*, 2008, **1**, 167– 174; c) Shaffer, D. W., Johnson, S. I., Rheingold, A. L., Ziller, J. W., Goddard, W. A.,Nielsen, R. J. and Yang, J. Y., *Inorg. Chem.*, 2014, **53**, 13031– 13041.

19a) Radosevich, A. T., Melnick, J. G., Stoian, S. A., Bacciu, D., Chen, C.-H.,Foxman, B. M., Ozerov, O. V. and Nocera, D. G., *Inorg. Chem.*, 2009, **48**, 9214– 9221; b) Adhikari, D., Mossin, S., Basuli, F., Dible, B. R., Chipara, M., Fan, H., Huffman, J. C., Meyer, K. and Mindiola, D. J., *Inorg. Chem.*, 2008, **47**, 10479– 10490; c) Davidson, J. J., DeMott, J. C., Douvris, C., Fafard, C. M., Bhuvanesh, N., Chen, C.-H., Herbert, D. E., Lee, C.-I., McCulloch, B. J., Foxman, B. M. and Ozerov, O. V., *Inorg. Chem.*, 2015, **54**, 2916– 2935; d) Vreeken, V., Siegler, M. A., Bruin, B., Reek, J. N. H., Lutz, M. and der Vlugt, J. I., *Angew. Chem. Int. Ed.*, 2015, **54**, 7055– 7059; *Angew. Chem.*, 2015, **127**, 7161; e) Wanniarachchi, S., Liddle, B. J., Toussaint, J., Lindeman, S. V., Bennett, B. andGardinier, J. R., *Dalton Trans.*, 2010, **39**, 3167– 3169; f) Wanniarachchi, S., Liddle, B. J., Toussaint, J., Lindeman, S. V., Bennett, B. andGardinier, J. R., *Dalton Trans.*, 2011, **40**, 8776– 8787.

20 The potentials in reference [21] were measured in propylene carbonate and reported vs. SCE. To adjust these values to the ferrocene reference, we used the fact that ferrocene has a potential of +0.38 V vs. SCE in propylene carbonate with $[NBu_4]PF_6$ as the electrolyte, as reported in reference [22].

21 James, T. L., Smith, D. M. and Holm, R. H., *Inorg. Chem.*, 1994, **33**, 4869– 4877.

22 Connelly, N. G. and Geiger, W. E., *Chem. Rev.*, 1996, **96**, 877– 910.

23 Adhikari, D., Mossin, S., Basuli, F., Huffman, J. C., Szilagyi, R. K., Meyer, K. andMindiola, D. J., *J. Am. Chem. Soc.*, 2008, **130**, 3676– 3682.

24 Klein, A., Vicic, D. A., Biewer, C., Kieltsch, I., Stirnat, K. and Hamacher, C., *Organometallics*, 2012, **31**, 5334– 5341.

25 Basu, D., Mazumder, S., Niklas, J., Baydoun, H., Wanniarachchi, D., Shi, X.,Staples, R. J., Poluektov, O., Schlegel, H. B. and Verani, C. N., *Chem. Sci.*, 2016, **7**,3264– 3278.

26a) Basu, D., Mazumder, S., Shi, X., Baydoun, H., Niklas, J., Poluektov, O.,Schlegel, H. B. and Verani, C. N., *Angew. Chem. Int. Ed.*, 2015, **54**, 2105– 2110; *Angew. Chem.*, 2015, **127**, 2133; b) Kankanamalage, P. H. A., Mazumder, S., Tiwari, V., Kpogo, K. K., Schlegel, H. B.and Verani, C. N., *Chem. Commun.*, 2016, **52**, 13357– 13360.

27a) Johnson, F. P. A., George, M. W., Hartl, F. and Turner, J. J., *Organometallics*,1996, **15**, 3374– 3387; b) Smieja, J. M., Sampson, M. D., Grice, K. A., Benson, E. E., Froehlich, J. D. andKubiak, C. P., *Inorg. Chem.*, 2013, **52**, 2484– 2491; c) Grice, K. A., Gu, N. X., Sampson, M. D. and Kubiak, C. P., *Dalton Trans.*, 2013, **42**,8498– 8503.

28a) Vollmer, M. V., Machan, C. W., Clark, M. L., Antholine, W. E., Agarwal, J.,Schaefer, H. F., Kubiak, C. P. and Walensky, J. R., *Organometallics*, 2015, **34**, 3– 12; b) Spall, S. J. P., Keane, T., Tory, J., Cocker, D. C., Adams, H., Fowler, H., Meijer, A. J. H. M., Hartl, F. and Weinstein, J. A., *Inorg. Chem.*, 2016, **55**, 12568– 12582.

29a) Lacy, D. C., McCrory, C. C. L. and Peters, J. C., *Inorg. Chem.*, 2014, **53**, 4980– 4988; b) Budzelaar, P. H. M., Bruin, B., Gal, A. W., Wieghardt, K. and Lenthe, J. H., *Inorg. Chem.*, 2001, **40**, 4649– 4655; c) Bruin, B., Bill, E., Bothe, E., Weyhermüller, T. and Wieghardt, K., *Inorg. Chem.*,2000, **39**, 2936– 2947.

30 Hoots, J. E., Rauchfuss, T. B. and Wrobleski, D. A., *Inorg. Synth.*, 1982, **21**, 175– 179.

31 Stoll, S. and Schweiger, A., *J. Magn. Reson.*, 2006, **178**, 42– 55.

32 Sheldrick, G. M., *Acta Crystallogr., Sect. A*, 2008, **64**, 112– 122.

33 Dolomanov, O. V., Bourhis, L. J., Gildea, R. J., Howard, J. A. K. and Puschmann, H., *J. Appl. Crystallogr.*, 2009, **42**, 339– 341.
34 Neese, F., ORCA - An Ab Initio, DFT and Semiempirical Electronic Structure Package, version 3.0, Max Planck Institute for Chemical Energy Conversion, Muelheim (Germany), 2013.
35a) Becke, A. D., *J. Chem. Phys.*, 1986, **84**, 4524– 4529; b) Perdew, J. P., *Phys. Rev. B*, 1986, **33**, 8822– 8824.
36a) Becke, A. D., *J. Chem. Phys.*, 1993, **98**, 5648– 5652; b) Lee, C. T., Yang, W. T. and Parr, R. G., *Phys. Rev. B*, 1988, **37**, 785– 789.
37a) Schafer, A., Huber, C. and Ahlrichs, R., *J. Chem. Phys.*, 1994, **100**, 5829– 5835; b) Schafer, A., Horn, H. and Ahlrichs, R., *J. Chem. Phys.*, 1992, **97**, 2571– 2577; c) Weigend, F. and Ahlrichs, R., *Phys. Chem. Chem. Phys.*, 2005, **7**, 3297– 3305.
38 Klamt, A. and Schueuermann, G., *J. Chem. Soc., Perkin Trans. 2*, 1993, 799– 805.
39a) Neese, F., *Curr. Opin. Chem. Biol.*, 2003, **7**, 125– 135; b) Neese, F., *J. Chem. Phys.*, 2001, **115**, 11080– 11096; c) Sinnecker, S., Neese, F., Noodleman, L. and Lubitz, W., *J. Am. Chem. Soc.*, 2004,**126**, 2613– 2622; d) Neese, F., *J. Chem. Phys.*, 2003, **118**, 3939– 3948.
40 The “core properties” basis set is derived from the TurboMole DZ basis set developed by Ahlrichs and co-workers. It was obtained from the basis set library under ftp.chemie.uni-karlsruhe.de/pub/basen.
41 Kutzelnigg, W., Fleischer, U. and Schindler, M., in: *The IGLO Method: Ab Initio Calculation and Interpretation of NMR Chemical Shifts and Magnetic Susceptibilities*, Vol. 23, Springer-Verlang, Heidelberg, 1990.
42 Yanai, T., Tew, D. P. and Handy, N. C., *Chem. Phys. Lett.*, 2004, **393**, 51– 57.
43a) Blaesi, E. J., Fox, B. G. and Brunold, T. C., *Biochemistry*, 2015, **54**, 2874– 2884; b) Fischer, A. A., Stracey, N., Lindeman, S. V., Brunold, T. C. and Fiedler, A. T., *Inorg. Chem.*, 2016, **55**, 11839– 11853; c) Fiedler, A. T. and Fischer, A. A., *JBIC J. Biol. Inorg. Chem.*, 2017, **22**, 407– 424.
44a) Hirata, S. and Head-Gordon, M., *Chem. Phys. Lett.*, 1999, **314**, 291– 299; b) Hirata, S. and Head-Gordon, M., *Chem. Phys. Lett.*, 1999, **302**, 375– 382.
45 Gagne, R. R., Koval, C. A. and Lisensky, G. C., *Inorg. Chem.*, 1980, **19**, 2854– 2855.